Microfluidic gas-flow profiling using remote-detection NMR

Christian Hilty*, Erin E. McDonnell, Josef Granwehr, Kimberly L. Pierce, Song-I Han†, and Alexander Pines

Materials Sciences Division, Lawrence Berkeley National Laboratory, Berkeley, CA 94720; and Department of Chemistry, University of California, Berkeley, CA 94720

Communicated by E. L. Hahn, University of California, Berkeley, CA, August 31, 2005 (received for review August 15, 2005)

We have used nuclear magnetic resonance (NMR) to obtain spatially and temporally resolved profiles of gas flow in microfluidic devices. Remote detection of the NMR signal both overcomes the sensitivity limitation of NMR and enables time-of-flight measurement in addition to spatially resolved imaging. Thus, detailed insight is gained into the effects of flow, diffusion, and mixing in specific geometries. The ability for noninvasive measurement of microfluidic flow, without the introduction of foreign tracer particles, is unique to this approach and is important for the design and operation of microfluidic devices. Although here we demonstrate an application to gas flow, extension to liquids, which have higher density, is implicit.

hyperpolarization | xenon | magnetic resonance imaging

Miniaturized fluid-handling devices have attracted considerable interest recently in many areas of science (1). Such microfluidic chips perform a variety of functions ranging from analysis of biological macromolecules (2, 3) to catalysis of reactions and sensing in the gas phase (4, 5). To enable precise fluid handling, accurate knowledge of the flow properties within these devices is important. Because of low Reynolds numbers, laminar flow is usually assumed. However, either by design or unintentionally, the flow characteristic in small channels is often altered (e.g., by surface interactions, viscous and diffusional effects, or electrical potentials). Therefore, its prediction is not always straightforward (6–8). Currently, most microfluidic flow measurements rely on optical detection of markers (9, 10), requiring the injection of tracers and transparent devices. Here we show profiles of microfluidic gas flow in capillaries and chip devices obtained by NMR in the remote-detection modality (11, 12). Through the transient measurement of dispersion (13), NMR is well adaptable for noninvasive yet sensitive determination of the flow field and provides a potentially more powerful tool to profile flow in capillaries and miniaturized flow devices.

NMR remote detection separates the encoding of NMR information from the detection of the actual signal. Information about a stationary object of interest is encoded into spin polarization of a mobile sensor by using radiofrequency (rf) pulses and field gradients. The spin sensor is then physically transferred to a different location for detection, which leads to a decisive enhancement of signal whenever geometrical constraints prevent the use of a sensitive NMR coil for detection directly at the sample site (11, 12). In the present work, we studied gas flow in model microfluidic devices by using hyperpolarized ^{129}Xe as a spin-carrying nucleus (14).

Experimental Procedures

Image information was encoded with an rf coil that completely encompassed the microfluidic device (Fig. 1). Such a coil arrangement ideally allows NMR-image information to be obtained from the entire microfluidic device. For measuring flow, it provides a decisive advantage over localized detection, which is achievable, for example, with microfabricated surface coils (15). However, the low filling factor on the order of 10^{-5} severely limits the obtainable signal and makes the acquisition of an NMR spectrum or image of gas in the conventional way unviable. With remote detection, the outflow of the fluid from the device can be used to carry the encoded information into a microsolenoid coil (16) wound around a capillary, which is connected to the outlet of the microfluidic device. The microcoil has a superior filling factor and is ideally suited to remotely retrieve the previously encoded information with a sensitivity gain of several orders of magnitude (E.E.M., S.-I.H., C.H., K.L.P., and A.P., unpublished data). Furthermore, remote detection uniquely provides the possibility of obtaining the axial dispersion of the fluid as an additional experimental dimension by recording the time of flight (TOF) between encoding and detection of individual spin packets. Thereby, the encoded signal is read out in a time-dependent manner (13), showing how fluid spreads as it travels through the device. The NMR-pulse sequence for the acquisition of these dispersion-resolved images is based on phase-encoded imaging (18) in the encoding coil, and a stroboscopic signal-detection scheme is applied on the microcoil to read out the axial dispersion (Fig. 2). The encoding step thus tags

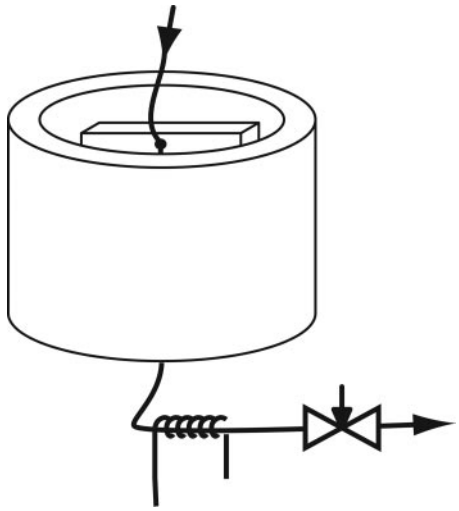

Fig. 1. Experimental setup for flow and dispersion measurements. A pressurized hyperpolarized xenon gas mixture containing 0.3% NMR-active ^{129}Xe [1% Xe at natural isotope abundance, 10% N_2, and 89% He at 5.6 atm (1 atm = 101.3 kPa) of delivery pressure], spin-polarized to 10%, is supplied from the top. It flows via a capillary through the microfluidic device to be profiled and exits at the bottom. The entire microfluidic device is surrounded by an assembly of magnetic field gradient and rf coils (3 × 4.5 cm) for encoding, and the outlet capillary leads through a microsolenoid (3 mm long, 400-μm inner diameter) for remote signal detection. The flow rate is controlled by an adjustable constriction at the outlet. The whole apparatus is inserted into the bore of a superconducting magnet (7 T).

*To whom correspondence should be addressed. E-mail: hilty@berkeley.edu.

†Present address: Department of Chemistry and Biochemistry, University of California, Santa Barbara, CA 93106-9510.

www.pnas.org/cgi/doi/10.1073/pnas.0507566102

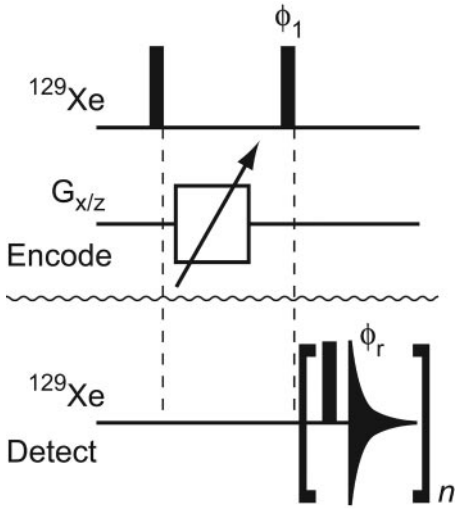

Fig. 2. Pulse sequence used for remote imaging of microfluidic flow. The top ^{129}Xe line and the line labeled $G_{x/z}$ show rf pulses at the frequency of ^{129}Xe and gradient pulses along the *x* and *z* axes, respectively, which are applied to the encoding volume. The pulse-sequence elements applied to the detection microcoil are shown on the lower ^{129}Xe line. Black bars represent 90° pulses, and the triangular shape symbolizes acquisition of one free induction decay. Phases are *x* unless otherwise noted; $\phi_1 = \phi_r = \{x, y, -x, -y\}$. On the encoding coil, the 90° pulse length is 90 μs, and the carrier frequency is set on-resonance with respect to the frequency of Xe gas. Gradient pulses are applied for 200 μs, with an additional recovery time of 10 μs. The gradient strength is varied in an array of otherwise identical experiments to obtain phase-encoded image information. On the encoding coils, the first rf pulse is for excitation of the target nuclei, the gradient pulses encode the image by adding a spatially dependent phase, and the second rf pulse stores the obtained intensity as longitudinal magnetization. For experiments with two spatial dimensions, gradients are applied along both the *x* and *z* axes, whereby for each *x*-gradient value, all *z*-gradient values are used. On the detection microcoil, the 90° pulse length is 0.65 μs, and the carrier frequency is set at 7 kHz off-resonance with respect to the frequency of Xe gas to avoid zero-frequency artifacts. The acquisition length for one single free induction decay determines the time resolution of the flow profiles and is set at or below the residence time of gas in the detection coil. The number of repetitions, *n*, is set such that the total acquisition time exceeds the longest time of travel of gas between the encoding and detection volumes. The flow profile, which is an image as a function of TOF between the locations of encoding and detection, is obtained by applying a complex Fourier transformation to each acquired free induction decay, integrating the real and imaginary part of each peak volume, and using the integrals corresponding to the same time of travel but different gradient strengths for a second complex Fourier transformation.

the fluid in a spatially dependent way without the need to insert a marker physically. Nuclear spins are ideal tracers, because they are naturally present in the fluid, and their state does not influence the flow properties in any way.

Results and Discussion

Fig. 3*A* shows the *z* profile of gas flowing from top to bottom through a straight capillary with a 150-μm inner diameter as a function of the TOF between encoding and detection. Immediately apparent is its slope, which represents the mean flow velocity inside the capillary, $v \approx 55$ cm·s^{-1}. The axial dispersion of the flow appears very small, as evidenced by a narrow distribution of travel times for any tagging location along the *z* direction. Such a pattern suggests a plug flow-like behavior and may at first glance seem contradictory to the expected laminar flow profile at a low Reynolds number of <10. However, this flow characteristic can be explained by the fast lateral diffusion of individual gas molecules, which diffuse across the channel in a very short time and efficiently sample all streamlines. The calculated (19, 20) and, by pulsed-field gradient NMR (21), experimentally determined diffusion constant of $D = 0.06$ cm^2·s^{-1} for ^{129}Xe at the given conditions translates to an average molecular displacement across 100 μm in $\approx$800 μs. The resulting dispersion profile reflects the combined effects of the laminar flow properties and lateral diffusion across the channel, which is fast compared to the total TOF between the encoding and detection location.

Figs. 3 *B* and *C* show profiles of axial dispersion that were obtained from a microfluidic glass chip with channels etched to a depth of 50 μm. The chip by design contains an enlargement of the channel width (*x* direction) but not of the depth. Its geometry was chosen to serve as a model for a microfluidic NMR sensor that, in the future, could be surface-activated by chemical or biological means. Between the two profiles, the chip geometry differs in that the chip used for Fig. 3*C* contained a mixing volume of 900 nl at the channel outlet (marked with a large open circle), which was not present in the chip used for Fig. 3*B*. The comparison between the two profiles demonstrates that this geometric difference leads to very distinct flow properties, which are discussed below. The inlet and outlet capillaries, with 150-μm inner diameters, were inserted perpendicular to the plane of the chip; therefore, they contained a short loop, which is seen for the outlet capillary at travel times $<$275 ms. At travel times above this value, the gas flowing inside the microfluidic chip is visible. In Fig. 3*B*, the different flow velocities in the narrow (travel times: 350–425 ms) and wide (travel times: 425–700 ms) sections of the device can be observed directly because of the different slopes of the trace in the profile. Above 775 ms, gas that remains for a long time in a mixing volume at the site of the connection to the inlet capillary can be observed. In contrast, in Fig. 3*C*, a substantial residence time is seen at the outlet mixing volume as well. Moreover, the signal shows forking at a travel time of 350 ms, with one branch being fed from the enlarged section of the channel as in Fig. 3*B* and the other branch caused by gas residing longer in the mixing volume. By measuring the length of the residence time until the forking occurs and the flow velocity, one can estimate the outlet volume that is effectively connected to the flow field to be $\approx$600 nl. Thus, the volume that gets exchanged only slowly, which is responsible for the stationary branch of the fork, is $\approx$300 nl. The observation of this forking emphasizes the complementary character of direct flow imaging (22–25) and TOF flow imaging. The former provides a map of local velocity vectors, whereas the latter is able to distinguish between different flow paths and shows how well a certain volume element is connected to the flow field. The smaller this connection is, the broader the dispersion profile and the weaker the signal becomes.

Flow profiles containing multiple spatial dimensions can be recorded by extending the experimental scheme described above to include pulsed-field gradients along multiple axes. Because of the two-dimensional nature of the device used for Fig. 3*B*, an additional data set was recorded with spatial resolution along *x* and *z*. With the TOF dimension available from the remote-detection scheme, this results in a three-dimensional data set. The five panels in Fig. 4*A* present a selection of images taken from this data set for different times of travel. Each panel is an image showing the spatially resolved origin of an ensemble of spins arriving in the detection coil at one time. The left-most panel with the shortest travel time, 470 ms, shows gas that was close to the outlet of the chip during encoding. Subsequently, gas flowing through the enlarged center section of the chip is seen, whereas the right-most panels contain intensity originating close to the inlet of the chip. A comparison reveals several details about the gas flow inside of the chip. For example, the first image shown from the wide section of the chip (540 ms) has a flat profile, whereas the

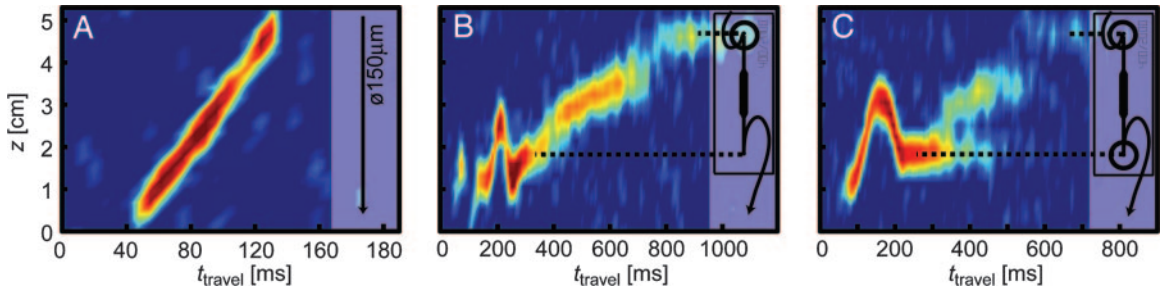

Fig. 3. Profiles of axial microfluidic flow dispersion. (*A*) Profile resolved in time of travel between the encoding and detection coil and along the *z* axis parallel to the magnetic field, obtained from a capillary with a 150-μm inner diameter. (*B*) Profile from a model microfluidic chip device containing a channel enlargement, directly connected to a capillary. (*C*) Profile from the same microfluidic chip connected to a capillary via a cylindrical volume of 900 nl. The gas was flowing in the direction of the negative *z* axis, with a flow rate set to $\approx$2.5 ml·min^{-1} (standard temperature and pressure) and a delivery pressure of 5.6 atm. The chip used for *B* and *C* consists of a channel that is 50 μm deep and 30 mm long. It is 400 μm wide at both ends but is enlarged to a width of 2,000 μm in the center. The positions along the long axis corresponding to the inlet and outlet of the chip are highlighted with dashed lines. Cavities with a volume of 900 nl between chip and capillary are marked with a large open circle in the drawings. Images were acquired in 3 h with a spatial resolution of 5.3 mm and a time resolution of 6 ms.

second image (610 ms) clearly shows a curvature of the profile across the channel, with the points containing intensity close to $x = \pm 1$ mm located further down in the channel than intensity-containing points close to $x = 0$ mm, which arises because of a difference in TOF between gas close to the edge ($x = \pm 1$ mm) and the center section ($x = 0$ mm). This curvature is indicative of a nonuniform velocity field inside the chip, which is not mixed effectively by transverse diffusion along the *x* dimension over the time scale of the gas flow through the chip. In the image showing gas at the position where the channel widens (680 ms), a nonuniform signal distribution is apparent, with a maximum at $x = 0$ and $z = 3.5$ cm and weaker intensity closer to the outlet and toward the edges. This pattern suggests that a certain fraction of gas from the section in the center of the channel reaches the outlet faster than average. Furthermore, when comparing this image with the image in which the channel narrows again (540 ms), it can be seen that gas spreads into the wide section ($z = 3.5$ cm) less rapidly than it condenses back into the narrow section ($z = 2.5$ cm). At $z = 3.5$ cm, the edges of the widening channel contain no intensity, indicating that gas in these locations is replaced less efficiently. This asymmetry may be even more easily visible in Fig. 4*B*, in which a sum of the intensity over all times of travel is shown. The effect of axial dispersion arising because of the flow properties inside of the chip is also readily visible when looking at time-resolved traces of gas originating from a specific position as it arrives at the detection coil. Fig. 4*C* shows three traces for gas inside of the microfluidic chip at different *z* positions. The amount of axial dispersion as the gas flows within the enlarged section of the chip is immediately apparent from the increasing width and decreasing height of the peaks for increasing distances to the outlet.

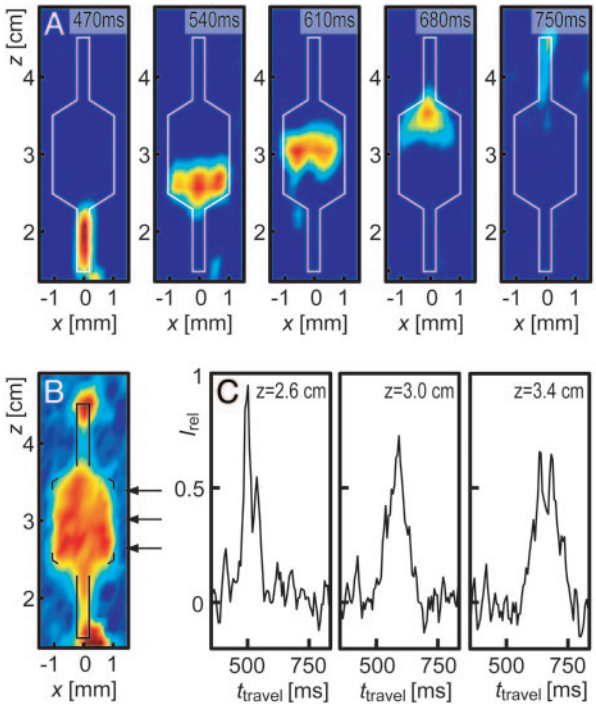

Fig. 4. Microfluidic flow resolved in two spatial dimensions parallel to the face of a microfluidic chip, along the *x* and *z* axes. (*A*) Five images of gas originating in the channel of the chip (outlined in white), shown for gas flowing from top to bottom, for different times of travel between the encoding location and detection coil. (*B*) Image of the perfused areas in the chip, reconstructed by summing the data shown in *A* over all travel times. (*C*) Three dispersion curves for gas originating at different *z* positions and $x = 0$ within the wide section of the chip. The positions of the traces are indicated with the arrows shown in *B*. The data were recorded in 9 h with a spatial resolution of 340 μm along the *x* direction and 2.7 mm along the *z* direction by using the same chip as in that used for Fig. 3*B*.

These results illustrate the ability to noninvasively study flow properties inside of microfluidic devices by NMR with TOF imaging. We profiled microfluidic gas flow, which was enabled despite the low spin density in a gas by using remote detection and hyperpolarized xenon as a spin-carrying tracer. An additional improvement of the sensitivity up to 2–3 orders of magnitude could be achieved by increasing the concentration of ^{129}Xe (26) and using a polarizer optimized for low mass flow (17). The same experiments can also be performed with liquids such as water and many organic solvents, in which nuclear spins that are already present in the liquid can be tagged during encoding. NMR provides several advantages compared to other methods for flow measurements, including freedom in the choice of the flow medium and the ability to work with opaque devices. With remote TOF imaging, foreign tracer substances that may be needed otherwise are not required, and microfluidic devices do not need to be designed specifically for NMR detection. The obtained axial dispersion profiles represent global characteristics of the entire flow path, which allows observing properties of the flow even when imaging with moderate spatial resolution compared to the channel size. In contrast to local velocity profiles, the data presented here show how individual points inside a microflu-

idic device are connected to the flow field and novel information is obtained about fluid velocities, mixing properties, and dispersion.

We thank Dr. Mahua Hajra for help with microfabrication and Prof. Richard Mathies for useful discussions. This work was supported by the Director of the Office of Science, Office of Basic Energy Sciences, Materials Sciences and Engineering Division, of the U.S. Department of Energy under contract DE-AC03-76SF00098. C.H. acknowledges support from the Schweizerischer Nationalfonds through a postdoctoral fellowship. Microfabrication was done in the Berkeley Microfabrication Laboratory (University of California, Berkeley).

1. Chovan, T. & Guttman, A. (2002) *Trends Biotechnol*. **20,** 116–122.
2. Burns, M. A., Johnson, B. N., Brahmasandra, S. N., Handique, K., Webster, J. R., Krishnan, M., Sammarco, T. S., Man, P. M., Jones, D., Heldsinger, D., *et al*. (1998) *Science* **282,** 484–487.
3. Huber, D. L., Manginell, R. P., Samara, M. A., Kim, B. I. & Bunker, B. C. (2003) *Science* **301,** 352–354.
4. Ueno, Y., Horiuchi, T., Morimoto, T. & Niwa, O. (2001) *Anal. Chem*. **73,** 4688–4693.
5. Kobayashi, J., Mori, Y., Okamoto, K., Akiyama, R., Ueno, M., Kitamori, T. & Kobayashi, S. (2004) *Science* **304,** 1305–1308.
6. Pathak, J. A., Ross, D. & Migler, K. B. (2004) *Phys. Fluids* **16,** 4028–4034.
7. Johnson, T. J., Ross, D. & Locascio, L. E. (2002) *Anal. Chem*. **74,** 45–51.
8. Stone, H. A., Stroock, A. D. & Ajdari, A. (2004) *Annu. Rev. Fluid Mech*. **36,** 381–411.
9. Singh, A. K., Cummings, E. B. & Throckmorton, D. J. (2001) *Anal. Chem*. **73,** 1057–1061.
10. Devasenathipathy, S., Santiago, J. G. & Takehara, K. (2002) *Anal. Chem*. **74,** 3704–3713.
11. Moulé, A. J., Spence, M. M., Han, S. I., Seeley, J. A., Pierce, K. L., Saxena, S. & Pines, A. (2003) *Proc. Natl. Acad. Sci. USA* **100,** 9122–9127.
12. Seeley, J. A., Han, S. I. & Pines, A. (2004) *J. Magn. Reson*. **167,** 282–290.
13. Granwehr, J., Harel, E., Han, S., Garcia, S., Pines, A., Sen, P. N. & Song, Y. Q. (2005) *Phys. Rev. Lett*. **95,** 075503.
14. Walker, T. G. & Happer, W. (1997) *Rev. Mod. Phys*. **69,** 629–642.
15. Massin, C., Boero, C., Vincent, F., Abenhaim, J., Besse, P. A. & Popovic, R. S. (2002) *Sens. Actuators A Phys*. **97-8,** 280–288.
16. Olson, D. L., Peck, T. L., Webb, A. G., Magin, R. L. & Sweedler, J. V. (1995) *Science* **270,** 1967–1970.
17. Knagge, K., Prange, J. & Raftery, D. (2004) *Chem. Phys. Lett*. **397,** 11–16.
18. Callaghan, P. T. (1991) *Principles of Nuclear Magnetic Resonance Microscopy* (Oxford Univ. Press, New York).
19. Hirschfelder, J. O., Curtiss, C. F. & Bird, R. B. (1954) *Molecular Theory of Gases and Liquids* (Wiley, New York).
20. Reid, R. C., Prausnitz, J. M. & Sherwood, T. K. (1977) *The Properties of Gases and Liquids* (McGraw–Hill, New York).
21. Stejskal, E. O. & Tanner, J. E. (1965) *J. Chem. Phys*. **42,** 288–292.
22. Kaiser, L. G., Logan, J. W., Meersmann, T. & Pines, A. (2001) *J. Magn. Reson*. **149,** 144–148.
23. Koptyug, I. V., Altobelli, S. A., Fukushima, E., Matveev, A. V. & Sagdeev, R. Z. (2000) *J. Magn. Reson*. **147,** 36–42.
24. Codd, S. L., Manz, B., Seymour, J. D. & Callaghan, P. T. (1999) *Phys. Rev. E Stat. Phys. Plasmas Fluids Relat. Interdiscip. Top*. **60,** R3491–R3494.
25. Zhang, X. F. & Webb, A. G. (2005) *Anal. Chem*. **77,** 1338–1344.
26. Mortuza, M. G., Anala, S., Pavlovskaya, G. E., Dieken, T. J. & Meersmann, T. (2003) *J. Chem. Phys*. **118,** 1581–1584.